

## Research papers

# Role of dielectric force and solid extraction in electrohydrodynamic flow assisted melting

R. Deepak Selvakumar<sup>a,b</sup>, Ahmed K. Alkaabi<sup>b</sup>, Jaiyoung Ryu<sup>c,\*</sup>, Hyoungsoon Lee<sup>a,d,\*\*</sup>

<sup>a</sup> School of Mechanical Engineering, Chung-Ang University, Seoul 06974, South Korea

<sup>b</sup> Department of Nuclear Engineering, Khalifa University of Science and Technology, Abu Dhabi, United Arab Emirates

<sup>c</sup> Department of Mechanical Engineering, Korea University Seoul, Seoul 02841, South Korea

<sup>d</sup> Department of Intelligent Energy and Industry, Chung-Ang University, Seoul 06974, South Korea



## ARTICLE INFO

## Keywords:

Melting  
Electrohydrodynamics  
Unipolar charge injection  
Heat transfer  
Phase-change material  
Energy storage

## ABSTRACT

A numerical study of non-isothermal solid-liquid phase change process in a differentially heated square cavity aided with an electrohydrodynamic (EHD) flow is reported. Melting of a phase change material (PCM) subjected to an electric field with different charge injection strengths is studied. The study aims to numerically demonstrate the solid extraction phenomenon and its role in accelerating the melting process. The EHD flow modifies the flow structure and notably alters the solid-liquid interface morphology. The dielectric force extracts the semi-solid PCM from the melt interface into the liquid bulk with high electric field intensity. The dielectric force causes melting-rate enhancement during the initial stages of melting. While, the later stages of melting are influenced by the combined action of Coulomb and dielectric forces. The role of the Coulomb force is weaker in the weaker charge-injection regimes. Higher electric potential and stronger charge injection generally lead to increased melting rates. Up to 62.12 % decrease in total time taken for melting is achieved within the parameters considered herein.

## 1. Introduction

Energy can be stored in the form of latent heat by melting and solidifying phase change materials (PCMs). Integration of latent heat thermal energy storage (LHTES) units into renewable energy systems is a popular technique to handle the intermittent availability of renewable energy and to manage supply-demand fluctuations. LHTES units offer advantages such as simple design & operation and high energy-to-volume ratio without significant energy loss [1–3]. Nevertheless, the PCMs used in LHTES systems possess low thermal conductivity. Hence, the energy storage rate is limited. Using additional flow to augment the heat transfer and, thereby, increasing the melting rate is a common active technique used in LHTES systems to increase the rate of energy storage [4,5].

Electrohydrodynamics (EHD) deals with the flow of a dielectric fluid medium subjected to an electric field. In the presence of an electric field, free charges in the dielectric medium move under the action of electric forces. Moving charges transfer momentum to the surrounding dielectric

fluid and induce a flow motion. EHD flow is popular among researchers as an active technique to increase heat transfer in single/two-phase flow systems [6–9]. Although EHD flow has been employed in fluid-fluid multiphase systems for heat transfer augmentation, its usage in systems dealing with solid-liquid phase change is relatively unexplored. The first experimental study of melting of paraffin wax in the presence of an applied electric field was performed by Nakhla et al. [10]. At the solid-liquid melt interface, the PCM was in a semi-solid state. Under the influence of electric field, the semi-solid PCM is pulled as dendrites into the liquid bulk. Nakhla et al. termed this phenomenon as “solid extraction” [10]. Subsequent experimental studies by dealt with the melting of n-octadecane subjected to an electric field [11–13]. Electroconvective flow induced by Coulomb force resulted up to 40.5 % speedup of melting process. Further experimental studies on EHD assisted melting of n-octadecane in different geometric configurations were performed by Sun et al. [14], provided more profound insights into the charge generation mechanisms. Strong electric fields led to charge generation by injection mechanism, and the conduction mechanism

\* Correspondence to: J. Ryu, School of Mechanical Engineering, Korean University, Seoul 02841, South Korea.

\*\* Correspondence to: H. Lee, School of Mechanical Engineering, Chung-Ang University, Seoul 06974, South Korea.

E-mail addresses: [jryu@korea.ac.kr](mailto:jryu@korea.ac.kr) (J. Ryu), [leeh@cau.ac.kr](mailto:leeh@cau.ac.kr) (H. Lee).

URL: <https://cfdlab.korea.ac.kr/> (J. Ryu), <https://atsla.cau.ac.kr/> (H. Lee).

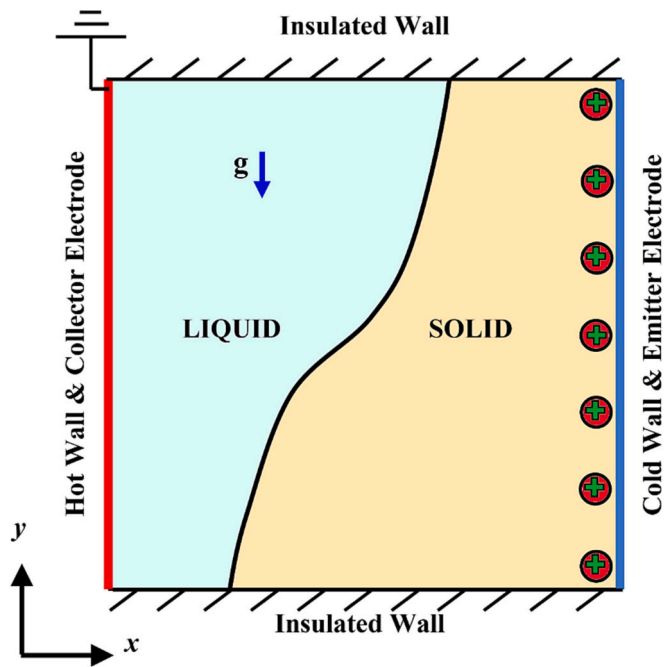


Fig. 1. Schematic representation the physical problem and the computational domain.

Table 1

Boundary conditions.

|                        | Top Wall<br>( $y = a$ ) | Bottom Wall<br>( $y = 0$ ) | Right Wall<br>( $x = a$ ) | Left Wall<br>( $x = 0$ ) |
|------------------------|-------------------------|----------------------------|---------------------------|--------------------------|
| Velocity $\vec{u}$     | $\vec{u} = 0$           | $\vec{u} = 0$              | $\vec{u} = 0$             | $\vec{u} = 0$            |
| Temperature $T$        | $\nabla T = 0$          | $\nabla T = 0$             | $T = 298.15 \text{ K}$    | $T = 343.15 \text{ K}$   |
| Charge Density $q$     | $\nabla q = 0$          | $\nabla q = 0$             | $q = q_0$                 | $\nabla q = 0$           |
| Electric Potential $V$ | $\nabla V = 0$          | $\nabla V = 0$             | $V = V_0$                 | $V = 0$                  |

dominated in weak/medium electric fields. The orientation of electric field and its interaction with thermal gradient affected the solid-liquid phase change process. Following the experimental works, Luo et al. [15] developed a numerical model for electric field assisted solid-liquid phase change process based on lattice Boltzmann method (LBM). Further parametric studies to investigate the flow instability in EHD assisted melting using the LBM approach were reported in refs. [16–18]. Selvakumar et al. [19] reported a finite-volume method (FVM) based numerical model for a solid-liquid phase change process subjected to unipolar charge injection under a strong electric field. Different stages and flow structures observed in the melting process subjected to electric field were identified. The mechanism of solid-liquid phase change process was highlighted. The combined effects of Coulomb and buoyancy forces and their interaction at different orientations were numerically investigated studied in refs. [20–23]. The orientation of grounded wall and the directions of electric field and thermal gradients resulted in different flow patterns and melting performances.

The electric field induces two main body forces: Coulomb and dielectric forces. The Coulomb force is a function of the distribution of free charges and the strength of the electric field. In contrast, the dielectric force is due to the variation of the dielectric permittivity of the material. Organic PCMs used in LHTES systems can be classified as pure paraffins and paraffin waxes. Pure paraffins have a very narrow melting-temperature range; thus, the melt interface is sharp. Hence, EHD-assisted melting of pure paraffin such as n-octadecane is governed only by the Coulomb force [11,12,14,20,24,25]. In contrast, paraffin waxes are impure substances with a wider melting-temperature range. As a result, they exhibit a thick semi-solid interface region. The

permittivity of semi-solid mushy region largely varies and thus, favors the action of dielectric force. Consequently, the solid extraction phenomenon is observed in the EHD-assisted melting of paraffin waxes, and the dielectric force plays a prime role in the melting-rate enhancement [10]. All LBM-based numerical studies [15–18,26] are based on the assumption of isothermal melting and consider only the Coulomb force. The FVM-based numerical study on the melting of n-octadecane [20] considers non-isothermal melting with both the Coulomb and dielectric forces. However, because pure paraffin (n-octadecane) was considered, the role of the dielectric force is insignificant. To the best of our knowledge, the role of the dielectric force and solid extraction phenomenon in the EHD-assisted melting of paraffin waxes is explored only in the experimental study reported by [10]. Numerical modeling of the solid extraction phenomenon in EHD-assisted melting of paraffin wax has not been reported in the literature. Paraffin waxes are more readily available and cheap than pure paraffin, like n-octadecane. Thus, the solid extraction phenomenon's mechanism and the dielectric force's role in the EHD-assisted melting of paraffin wax deserve further exploration. The present work aims to numerically demonstrate the solid extraction phenomenon and analyze its role in the EHD-assisted melting of paraffin wax in a square capsule. Furthermore, the effect of charge-injection strength in the EHD-assisted melting remains unexplored. The present study also considers the impact of electric forces under different charge injection strengths varying in weak, medium, and strong regimes.

## 2. Mathematical formulation of the problem

A differentially heated square cavity of size  $a = 30 \text{ mm}$  is taken into account. Initially, the cavity is filled with solid paraffin wax at room temperature  $T_\infty = 298.15 \text{ K}$ . The left wall is electrically grounded ( $V_0 = 0 \text{ kV}$ ) and considered the hot wall with a constant high-temperature  $T_H = 343.15 \text{ K}$ . The right boundary is maintained at ambient temperature  $T_\infty = 298.15 \text{ K}$  and also serves as the high voltage electrode ( $V_0 > 0 \text{ kV}$ ). Injection charge density  $q_0$  is considered at the emitter electrode surface [27]. The charge injection is uniform throughout the high voltage electrode surface [28]. The horizontal walls are adiabatic and electrically insulated. The no-slip boundary condition is applied for velocity in all cavity walls. A schematic sketch of the flow problem considered herein is shown in Fig. 1, and the corresponding boundary conditions are given in Table 1. The numerical model is based on the following assumptions:

- (1) 2D, laminar, and incompressible Newtonian flow is considered.
- (2) Volumetric expansion is considered to be negligible.
- (3) Temperature dependence of material properties and Joule-heating effects are neglected [27,29,30].
- (4) Density variation is modeled based on the Boussinesq approximation.

### 2.1. Governing equations

The melting process of paraffin wax subjected to unipolar charge injection induced EHD flow is considered. The electric forces influences the flow field, and the flow field affects the charge density distribution. The governing equations considering the two-way coupled EHD melting process are given as follows [15,19,20,26]:

Continuity equation:

$$\nabla \cdot \vec{u} = 0 \quad (1)$$

Momentum equation:

$$\frac{\partial \vec{u}}{\partial t} + \nabla \cdot (\vec{u} \vec{u}) = -\nabla p + \nu \nabla^2 \vec{u} - \vec{g}[1 - \beta(T - T_\infty)] + \vec{F}_e \quad (2)$$

Here,  $\vec{u} = [u_x, u_y]$  denotes the vector field of flow velocity, and  $\vec{g} =$

**Table 2**  
List of thermophysical and electric properties of paraffin wax.

| Property  | Value (Solid/Liquid)                                  |
|---|---|
| Density [ $\text{kgm}^{-3}$ ]                             | 870/760 [32]  |
| Thermal conductivity [ $\text{Wm}^{-1}\text{K}^{-1}$ ]    | 0.24/0.15 [32]  |
| Specific-heat capacity [ $\text{Jkg}^{-1}\text{K}^{-1}$ ] | 2400/1800 [32]  |
| Latent heat [ $\text{Jkg}^{-1}$ ]                         | $192 \times 10^3$ [10]                                |
| Solidus temperature [K]                                   | 326.15 [10]   |
| Liquidus temperature [K]                                  | 336.15 [10]   |
| Volumetric expansion coefficient [ $\text{K}^{-1}$ ]      | 0.00074 [10]  |
| Dynamic viscosity [ $\text{kgm}^{-1}\text{s}^{-1}$ ]      | $3.42 \times 10^{-3}$ [32]                            |
| Dielectric permittivity [ $\text{Fm}^{-1}$ ]              | $1.992 \times 10^{-11}/1.771 \times 10^{-11}$ [10,39] |
| Ionic mobility [ $\text{m}^2\text{s}^{-1}\text{V}^{-1}$ ] | $4.39 \times 10^{-8}/4.39 \times 10^{-9}$ [29]        |

$\vec{g}$  ( $g > 0$ ) represents the gravitational acceleration.  $\vec{e} = [0, 1]$ ,  $p$  and  $\nu$  are the unit surface normal vector, pressure, and kinematic viscosity, respectively.  $\vec{g}[1 - \beta(T - T_\infty)]$  in Eq. (2) is the gravitational body-force term calculated by Boussinesq approximation, where  $\beta$  is the coefficient of thermal expansion.  $\vec{F}_e$  is the electric body force which is expressed as follows [6]:

$$\vec{F}_e = q\vec{E} + \frac{1}{2}|\vec{E}|^2\nabla\epsilon. \quad (3)$$

The Coulomb force  $q\vec{E}$  depends on the charge density distribution and electric field and it acts on the liquid bulk. The dielectric force  $\frac{1}{2}|\vec{E}|^2\nabla\epsilon$  acts due to the permittivity gradient in the interface region. The dielectric force acts in a normal direction to the interface, toward the region of high electric-field intensity. The body force term  $\vec{F}_e$  due to electric field can be obtained by the solution of equations for electric potential, electric field and charge transport equations [27,30]. Electric field  $\vec{E}$  is given by the gradient of electric potential  $V$ .

$$\vec{E} = -\nabla V \quad (4)$$

Poisson equation of the electric potential:

$$\nabla \cdot (\epsilon \nabla V) = -q \quad (5)$$

Charge transport equation

$$\frac{\partial q}{\partial t} + \nabla \cdot \vec{J} = 0. \quad (6)$$

$\vec{J}$  indicates the current density vector and is calculated as

$$\vec{J} = K\vec{E} \cdot q + \vec{u} \cdot q - D\nabla q. \quad (7)$$

In Eq. (5),  $\epsilon$  and  $q$  are the dielectric permittivity of the material and local charge density, respectively.  $K\vec{E} \cdot q$  represents the electromigration of the charges due to ionic mobility of the dielectric medium, and  $K \cdot \vec{u} \cdot q$  describes the convection of the charge density by the flow velocity field. The charge diffusion  $D\nabla q$  is due to ionic diffusivity  $D$ . Ionic diffusivity of dielectric materials is negligible [6,29].

A single energy equation for both solid and liquid phase in terms of enthalpy is solved to obtain the temperature distribution as follows [31]:

Energy equation:

$$\rho \frac{\partial H}{\partial t} + \rho \nabla \cdot (\vec{u} H) = \nabla \cdot (k \nabla T). \quad (8)$$

Here,  $\rho$  and  $k$  are the density and thermal conductivity of the PCM.  $T$  denotes the temperature, and  $H = c_p T + \Delta H$  gives the total enthalpy in each computational cell.  $c_p$  is the specific heat capacity, and the total sensible heat content in each control volume is provided by  $c_p T$ . Change in enthalpy  $\Delta H$  is the latent-heat content in every cell in the computational domain.  $\Delta H$  is dependent on local temperature as follows:

$$\Delta H = \begin{cases} 0, & T < T_s \\ L \left[ \frac{T - T_s}{T_l - T_s} \right], & T_s \leq T \leq T_l \\ L, & T \geq T_l \end{cases}. \quad (9)$$

$L$  is the latent heat of fusion.  $T_l$  and  $T_s$  denote the liquidus and solidus temperatures, respectively. Any control volume is considered to be in solid, liquid, or semi-solid state at a given instantaneous time moment based on the local latent heat content.  $\Delta H = L$  or  $0$  indicates that the cell is in the liquid or solid state. Cells with  $\Delta H$  having intermediate values between  $0$  and  $L$  are in a semi-solid state that form the melt interface. Thus, the local liquid fraction in each control volume is denoted by  $f_l = \Delta H/L$ . From Eq. (9),

$$f_l = \begin{cases} 0, & T < T_s \\ \left[ \frac{T - T_s}{T_l - T_s} \right], & T_s \leq T \leq T_l \\ 1, & T \geq T_l \end{cases}. \quad (10)$$

Combining Eqs. (8)–(10), the energy equation is written as

$$\rho \frac{\partial c_p T}{\partial t} + \rho \nabla \cdot (\vec{u} c_p T) = \nabla \cdot (k \nabla T) - \rho \left[ \nabla \cdot (\vec{u} \Delta H) + \frac{\partial \Delta H}{\partial t} \right]. \quad (11)$$

Eq. (11) is further simplified as

$$\frac{\partial T}{\partial t} + \rho \nabla \cdot (\vec{u} T) = \nabla \cdot (\alpha \nabla T) + S_T. \quad (12)$$

Eq. (11) is further simplified as  $S_T = - \left[ \nabla \cdot (\vec{u} \cdot (L f_l)) + \frac{\partial (L f_l)}{\partial t} \right] / c_p$  is the enthalpy-source term [31–34]. A smooth velocity transformation from a finite value in the liquid region to zero in the solid region is obtained by the momentum-source term  $S_m = A \vec{u}$ .  $A$  is the porosity function used in Carman–Kozeny equation [35] that describes a flow in porous media, which is given by

$$A = -\gamma \frac{(1 - f_l)^2}{f_l^3 + \aleph}. \quad (13)$$

Here,  $\gamma = 1 \times 10^6$  is the interface morphology constant [36], and  $\aleph = 10^{-6}$  is a small constant used to avoid division by zero [19,20,31]. When  $f_l = 1$ , the momentum source becomes zero, and solving momentum equation calculates the velocity. When  $f_l = 0$ ,  $\gamma$  ultimately nullifies the velocity owing to its large value. The semi-solid interface region undergoes a smooth velocity transformation as a function of the local liquid fraction. Thus, the momentum equation with the source term is

$$\frac{\partial \vec{u}}{\partial t} + \nabla \cdot (\vec{u} \vec{u}) = -\nabla p + \nu \nabla^2 \vec{u} - \vec{g}[1 - \beta(T - T_\infty)] + \vec{F}_e + S_m. \quad (14)$$

## 2.2. Boundary conditions

Table 1. presents the boundary values employed to solve the governing equations. Firstly, the boundary condition for charge density  $q_0$  at the high voltage electrode surface has to be discussed in detail. Experimental measurement of charge injection intensity from an electrode surface is not possible. Thus, an injection parameter  $C = \frac{q_0 a^2}{\epsilon_1 \Delta V}$  measures charge-injection strength [29].  $C$  can be varied at three levels, namely, 0.1, 1, and 10, representing charge injection in weak, medium, and strong regimes. Thus, the boundary condition for charge-density  $q_0$  at the emitter electrode surface is calculated based on the expression for injection parameter and applied electric potential. Two levels of applied voltage  $V_0 = 10$  and  $20$  kV are considered in the weak ( $C = 0.1$ ), medium ( $C = 1$ ), and strong ( $C = 10$ ) injection regimes.

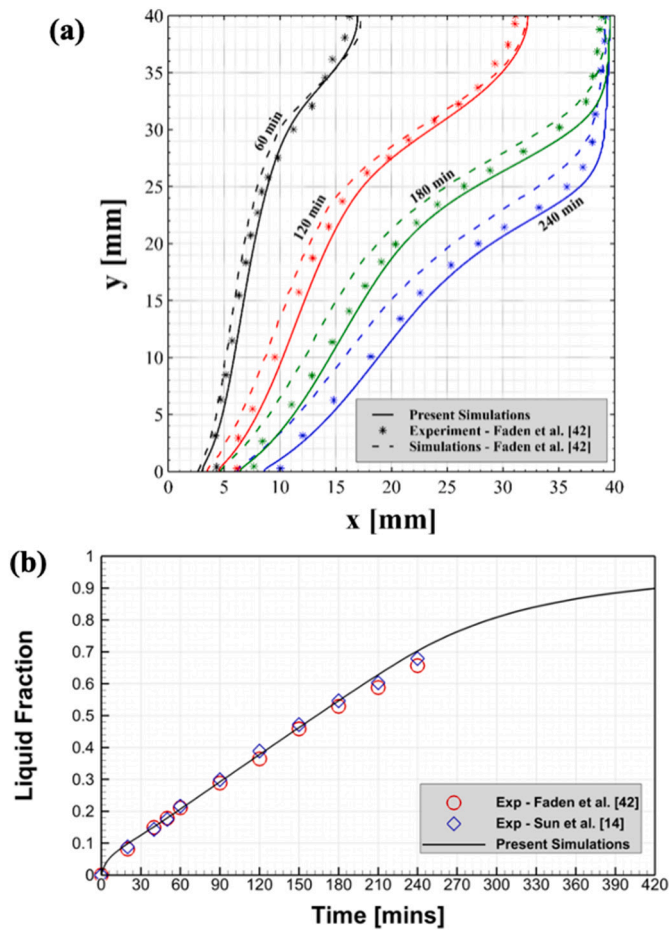


Fig. 2. Melting of n-octadecane in a differentially heated square cavity without an electric field. (a) Melt interface position and (b) Evolution of liquid fraction [14,42].

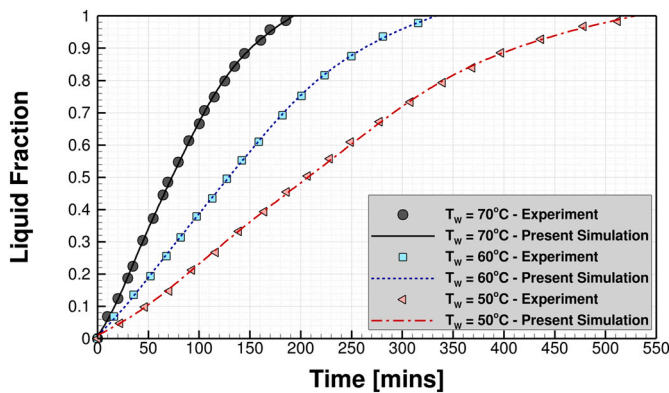


Fig. 3. Comparison of present numerical prediction of growth in liquid volume fraction with respect to time in melting of lauric acid with the data reported in Ref. [43].

### 2.3. Thermophysical and dielectric properties

The thermophysical and dielectric properties of the PCM (paraffin wax) in solid and liquid phases are given in Table 2. Solid and liquid PCM's thermophysical and electric properties are different but constant for a given phase. The dielectric properties of organic PCMs show negligible variation with respect to temperature [37]. The material properties are defined as a function of the local liquid fraction. Walden's

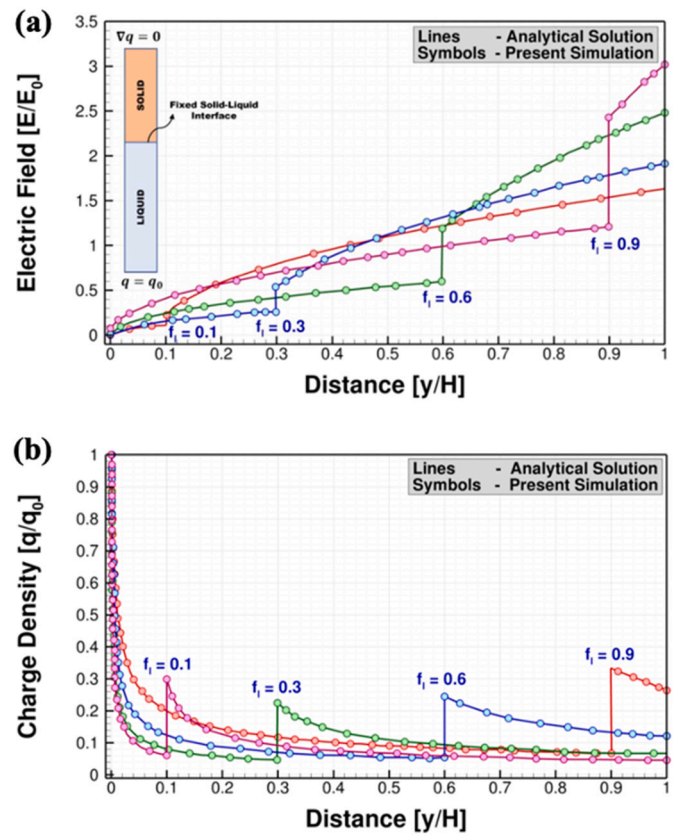


Fig. 4. Comparison between the present numerical results and 1D hydrostatic analytical solution. Evaluation conducted for space charge transport across a solid-liquid interface in the presence of electric field [15]. (a) Electric-field profile and (b) Distribution of charge density.

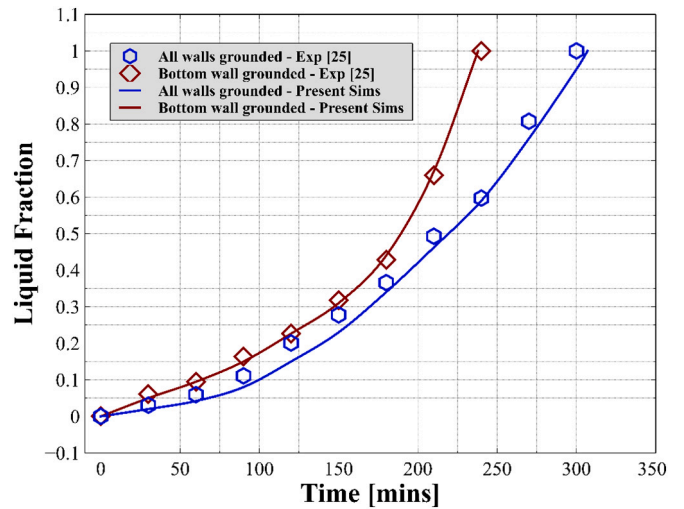


Fig. 5. Melting in the presence of electric field. Present numerical results for increase in liquid fraction with respect to time are compared with experimental data from literature [25].

rule [29,38] is utilized to calculate the ionic mobility of paraffin wax in the liquid state.

$$K = \frac{1.5 \times 10^{-11}}{\mu} [m^2 s^{-1} V^{-1}]. \quad (15)$$

Here,  $\mu$  represents the viscosity. The ratio of ionic mobility of the

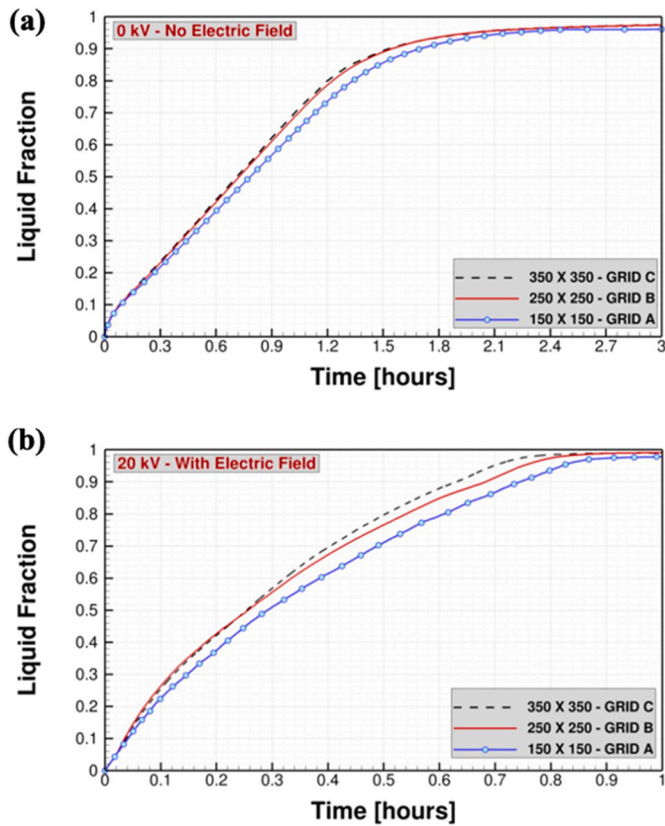


Fig. 6. Results of the grid-sensitivity analysis of the melting of paraffin wax in a square cavity. (a) Without an electric field (0 kV) and (b) With an electric field (20 kV).

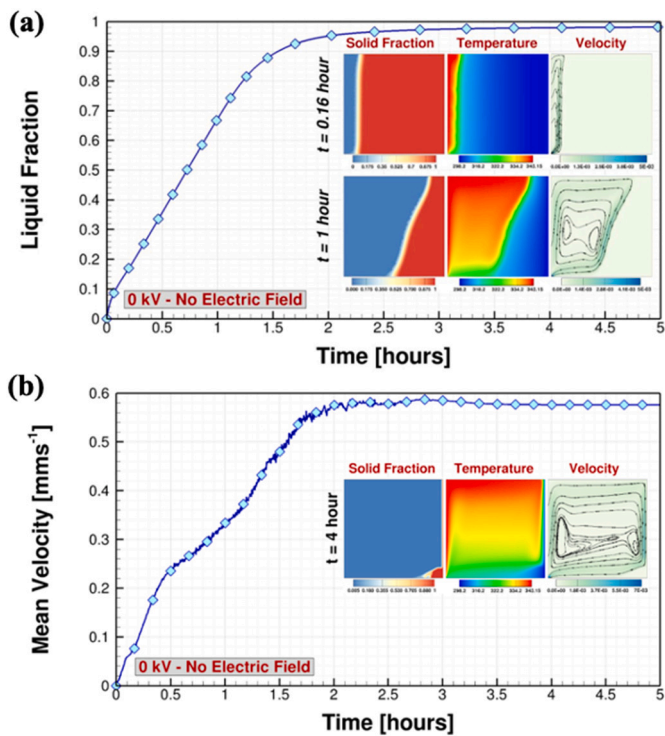


Fig. 7. Melting of paraffin wax without electric field ( $V = 0$  kV). (a) Melting rate curve and (b) Variation of mean velocity with respect to time. (The inset images show the solid fraction distribution, thermal field, and flow velocity with streamlines.)

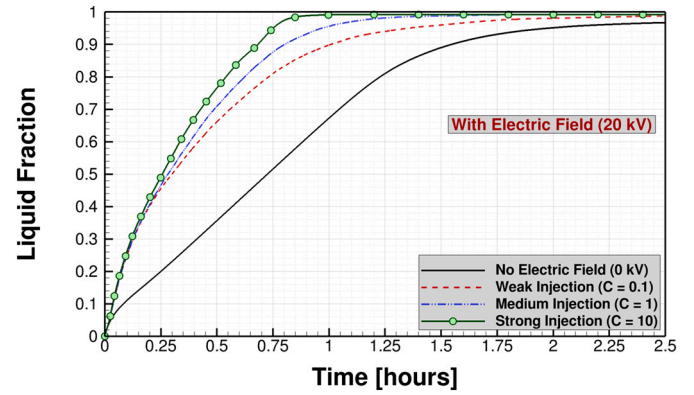


Fig. 8. Growth of the liquid fraction with time in EHD-assisted melting of paraffin wax in the weak ( $C = 0.1$ ), medium ( $C = 1$ ), and strong ( $C = 10$ ) injection regimes and at an applied voltage of 20 kV.

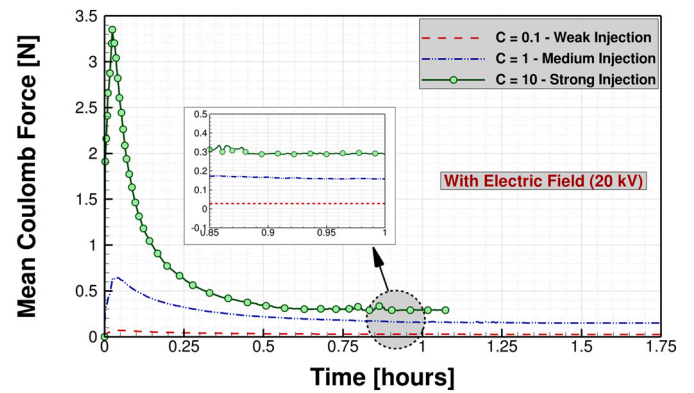


Fig. 9. Variation of mean Coulomb force with time in EHD-assisted melting of paraffin wax in the weak ( $C = 0.1$ ), medium ( $C = 1$ ), and strong ( $C = 10$ ) injection regimes and at an applied voltage of 20 kV.

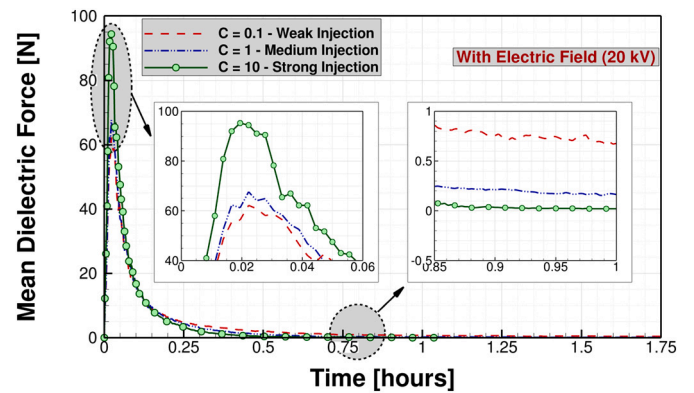


Fig. 10. Time evolution of the mean dielectric force during the EHD-assisted melting of paraffin wax in the weak ( $C = 0.1$ ), medium ( $C = 1$ ), and strong ( $C = 10$ ) injection regimes and at an applied voltage of 20 kV.

PCM in solid state to its value in liquid state is equal to 10 [37].

### 3. Numerical methodology and code validation

#### 3.1. Numerical approach

Finite-volume method (FVM) framework of OpenFOAM® is used to solve the governing equations. The governing equations are discretized

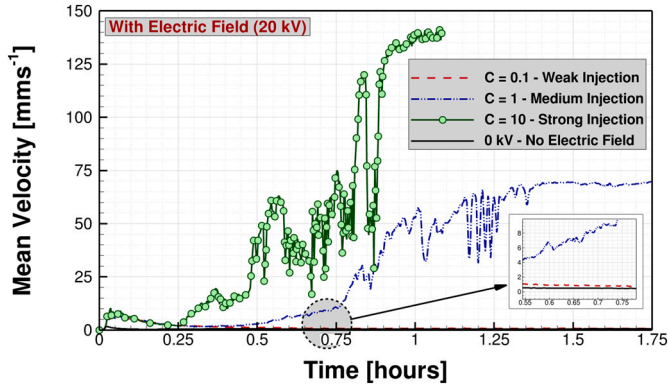


Fig. 11. Time evolution of the mean velocity during the EHD-assisted melting of paraffin wax in the weak ( $C = 0.1$ ), medium ( $C = 1$ ), and strong ( $C = 10$ ) injection regimes and at an applied voltage of 20 kV.

in a 2D uniform grid using the in-built finite-volume procedures of OpenFOAM® [40]. A second-order accurate linear scheme is used to discretize the Laplacian terms. Convective terms are discretized using second-order upwind scheme. The term representing the electromigration of charges in Eq. (7) is modified into a conventional convective term as follows:

$$\nabla \cdot (qK\vec{E}) = \nabla \cdot (q\vec{\omega}). \quad (16)$$

$\omega_f = (K\vec{E})_f \cdot S_f = -(K\nabla V)_f \cdot S_f$  is the electromigration flux and is calculated on each cell face.  $S_f$  is the surface normal vector with a magnitude equal to the area of the corresponding cell face. Thus, the electromigration term can be implicitly discretized. The negligible ionic diffusion results in a hyperbolic charge transport equation [29]. A total variation diminishing (TVD) VanLeer scheme [41] coupled with deferred correction approach is used to discretize the advective terms in the charge transport equation. The temporal derivatives are discretized using the Crank Nicolson Scheme with a coefficient equal to 0.9. The sparse matrices obtained by the discretization procedures are solved using the stabilized preconditioned bi-conjugate gradient (PGiCGStab) method with simplified diagonal-based incomplete Cholesky preconditioner. Symmetric matrices resulting from the discretization procedures are solved by the geometric-algebraic multigrid (GAMG) method with Gauss-Seidel preconditioner. The iterative solution at each time step is considered to be converged when the residuals for all variables fall below  $1 \times 10^{-7}$ .

### 3.2. Code validation

The physical problem considered herein combines two basic mechanisms, (i) melting due to natural convection and (ii) electric-field-coupled space charge transport across a solid-liquid interface. Firstly, the present numerical solver developed in OpenFOAM® is tested for its ability to handle these two fundamental problems. Finally, current numerical results are compared with the experimental data for charge injection induced EHD flow assisted melting.

#### 3.2.1. Convective melting

In this section, we compare results from the present numerical solver for pure natural convection melting with experimental results reported in literature. The benchmark data from the literature [14,42] considers melting of n-octadecane in a differentially heated cavity with sides of length 40 mm. Fig. 2 (a) compares the shape and location of the solid-liquid melt interface at different instantaneous time moments obtained in present simulations with the experimental results. The interface shape predicted by present numerical simulations shows a good qualitative match with the literature data. Likewise, the growth of liquid fraction

with respect to time is mapped in Fig. 2 (b). Present numerical results match well with the experimental data from the literature. In addition, the transient increase in liquid fraction during lauric acid melting process calculated by the current numerical solver is shown in Fig. 3. The comparison with the previously reported data in ref. [43] shows a good match.

#### 3.2.2. Space-charge transport across a solid-liquid interface

The present section reports the ability of the numerical solver to simulate space charge transport across a fixed solid-liquid interface in the presence of an electric field. The analytical solutions for the space charge density distribution and electric field distribution in a 1D hydrostatic domain with a solid-liquid interface were derived by [15] as follows:

$$E_l = a(y + b)^{0.5} \quad (17)$$

$$q_l = \frac{a}{2C(y + b)^{0.5}} \quad (18)$$

$$E_s = c(y + d)^{0.5} \quad (19)$$

$$q_s = \frac{c}{2C\epsilon_r(y + d)^{0.5}} \quad (20)$$

$a$ ,  $b$ ,  $c$ , and  $d$  are arbitrary constants defined by Luo et al. [15].  $C = 10$  represents the injection parameter. The difference in liquid and solid electric properties are defined by the permittivity ratio  $\epsilon_r = \epsilon_l/\epsilon_s = 2$  and mobility ratio  $K_r = K_l/K_s = 10$ . Figs. 4 (a) and (b) show that the present numerical results show excellent agreement with the analytical solutions. More importantly, sharp gradients in the proximity of the high voltage electrode and the step change across the interface are obtained with almost no numerical diffusion and without any un-physical oscillations.

#### 3.2.3. Melting with charge injection induced EHD flow

Finally, a case of EHD assisted melting of n-octadecane in a 2D square cavity with a circular wire electrode is considered. The charge injection takes place from the high voltage ( $-25$  kV) wire electrode. The geometrical dimensions of the computational domain and the relevant boundary conditions are set based on the experimental setup used by Sun et al. [25]. Two cases are considered here, with the first case with a grounded bottom wall and the second one having all four cavity walls as grounded electrodes. The conditions adopted in the experiment confirmed charge injection at an electric field strength in the range of  $1 \times 10^6$  V/m. The electric field intensity in the simulations performed in this study is also in the same order; hence, the assumption of charge injection from the high-voltage electrodes is valid. The growth of liquid volume fraction in the square cavity obtained by present numerical simulations is compared with the results of ref. [25] in Fig. 5. For both cases, the current numerical prediction matches well with the experimental results, with a maximum deviation  $< 4\%$ .

It is to be noted that in any experimental study of melting, the PCM will undergo volumetric thermal expansion and there will be trapped air bubbles in the PCM. These physical phenomena are not considered in the numerical model employed in this study, to avoid complexity. The objective of the present study is to investigate the effect of Coulomb and dielectric forces acting in the bulk liquid PCM and the interface. The validation cases considered in this section confirm the ability of the customized numerical solver developed in OpenFOAM® to model the melting of PCM assisted with EHD flow induced by unipolar charge injection. Even without the consideration of volumetric expansion and trapped air, the numerical model is able to produce results that match well with the experimental data from literature. Moreover, numerical model for melting without considering the volumetric expansion of PCM and trapped air is common in literature [44,45].

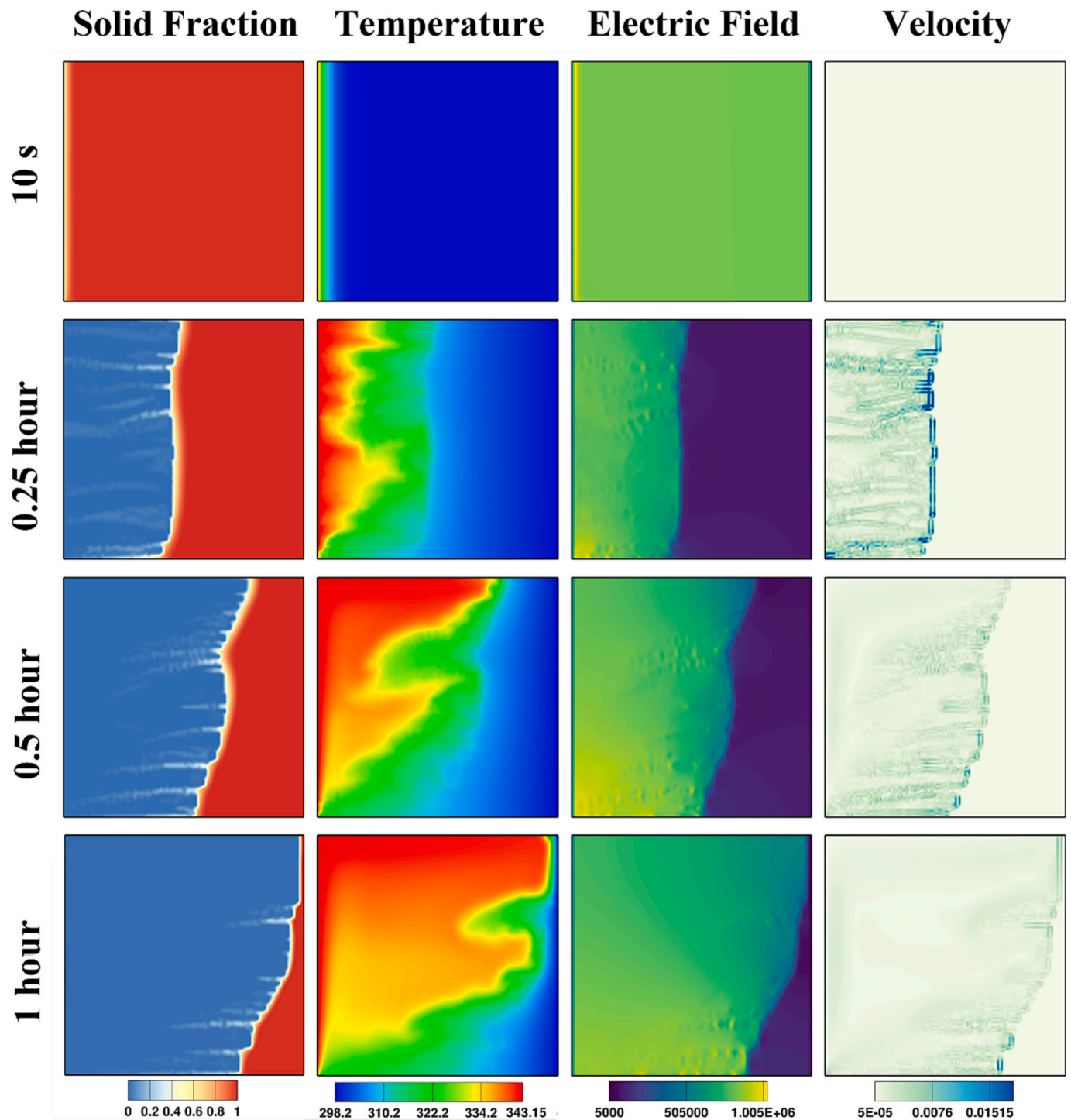


Fig. 12. Solid fraction distribution, thermal field, electric-field, and velocity at different instantaneous moments during the EHD-assisted melting of paraffin wax in a square capsule. The applied electric potential is 20 kV in a weak charge-injection regime ( $C = 0.1$ ).

#### 4. Grid-sensitivity analysis

The growth of liquid volume fraction with respect to time using three grids (A, B, and C) is presented in Fig. 6. Two cases, namely, (i) pure natural convection melting (0 kV) and (ii) EHD assisted melting ( $V_0 = 20$  kV) and  $C = 10$ , are considered. Initially, for a short period the heat transfer is mainly due to conduction and hence, the melting curves using the three grids are coincident with each other. With the progress of time, fluid motion begins, and the melting curves of different grids begin to show variations. The variation between grids B and C is minimal and

within acceptable limits. For the case without electric field (refer Fig. 6 (a)), the curves of grid B and C closely match with each other. For the case with electric field presented in Fig. 6(b), the maximum deviation is only 2.6 % which is noted in the later stages of melting, where the liquid fraction is 0.9. Considering the accuracy, stability, and computational expenses, grid B with 250 uniform cells in the horizontal and vertical directions is selected for all the 2D simulations presented in this study. All the simulations performed in this study are transient in nature. Adaptive time stepping is used with a limiting Courant number equal to 1.0 and a maximum time step size equal to 0.0001 s.

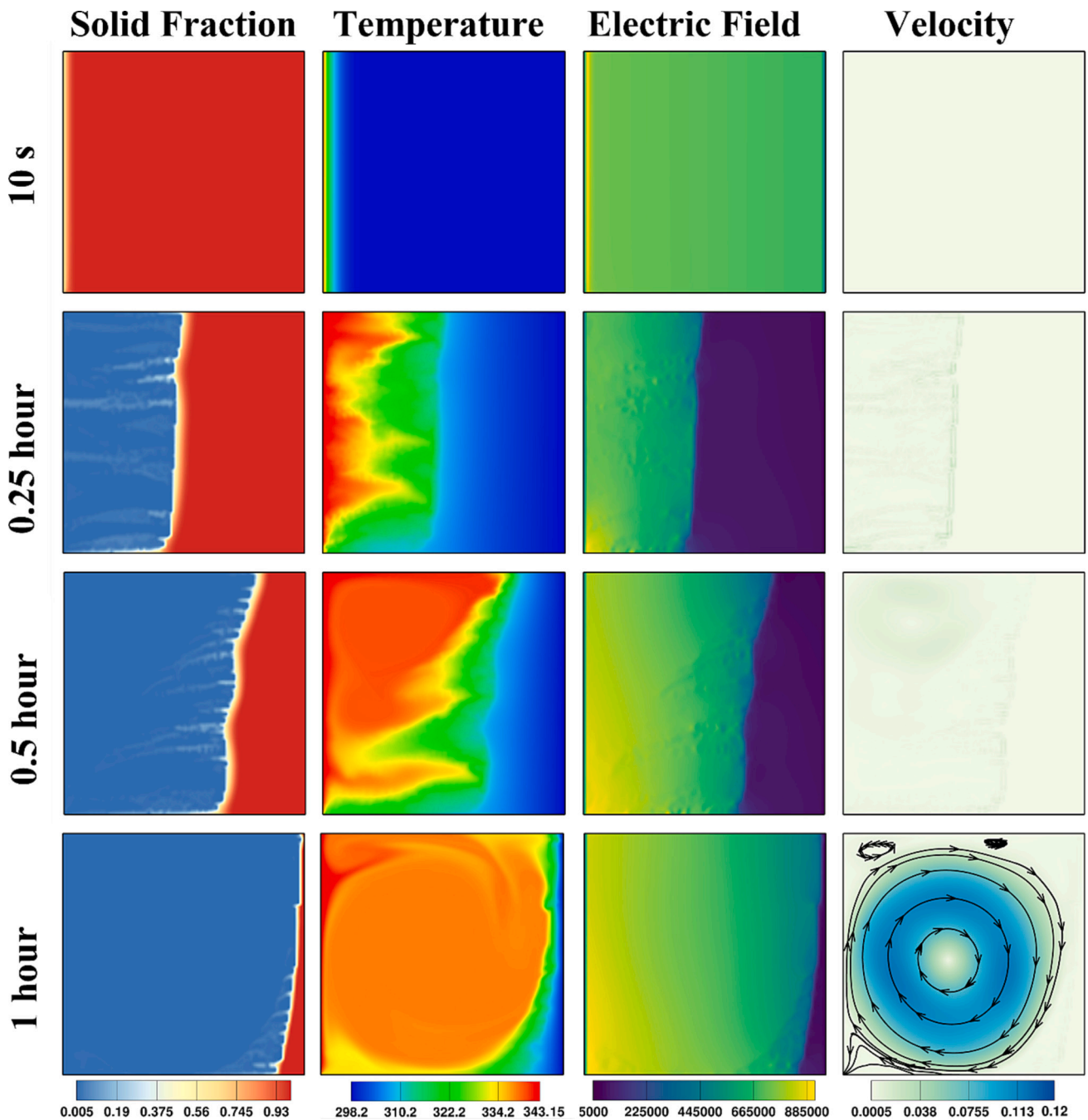


Fig. 13. Solid fraction distribution, thermal field, electric-field, and velocity at different instantaneous moments during the EHD-assisted melting of paraffin wax in a square capsule. The applied electric potential is 20 kV in a medium charge-injection regime ( $C = 1$ ).

## 5. Results and discussion

Numerical simulations of the melting of paraffin wax in a square capsule assisted with EHD flow induced by unipolar charge injection in the presence of an external electric field are presented in this section. The benchmark is first set up by considering a case without an electric field, where the melting is only due to natural convective flow motion. Subsequently, the influence of unipolar charge injection under two applied voltages (10 and 20 kV) and in the weak ( $C = 0.1$ ), medium ( $C = 1$ ), and strong ( $C = 10$ ) charge injection regimes are investigated. The physical mechanism of solid extraction and its role in enhancing the melting rate is elaborated. Finally, the same problem is investigated using a three-dimensional (3D) computational domain to obtain better visualization and understanding of the solid extraction phenomenon.

### 5.1. Melting without electric field

Firstly, establishing the flow structure and melting behavior in a buoyancy-driven melting process is essential. Fig. 7(a) shows the time evolution of the total liquid fraction in the computational domain, and Fig. 7(b) shows the mean velocity in the fluid region. Moreover, the contours of the solid fraction, temperature, and velocity with streamlines are shown as inset images. The liquid fraction increases as the melting process begins from the heated left wall. The conduction heat transfer primarily governs the initial melting process. Until  $t < 0.16$  h, the melt interface remains approximately parallel to the heated wall, and the mean-velocity distribution is weak, which confirms the conduction-dominated melting process. At  $t \geq 0.16$  h, the upper edge of the solid-liquid interface begins to lean toward the right wall, which

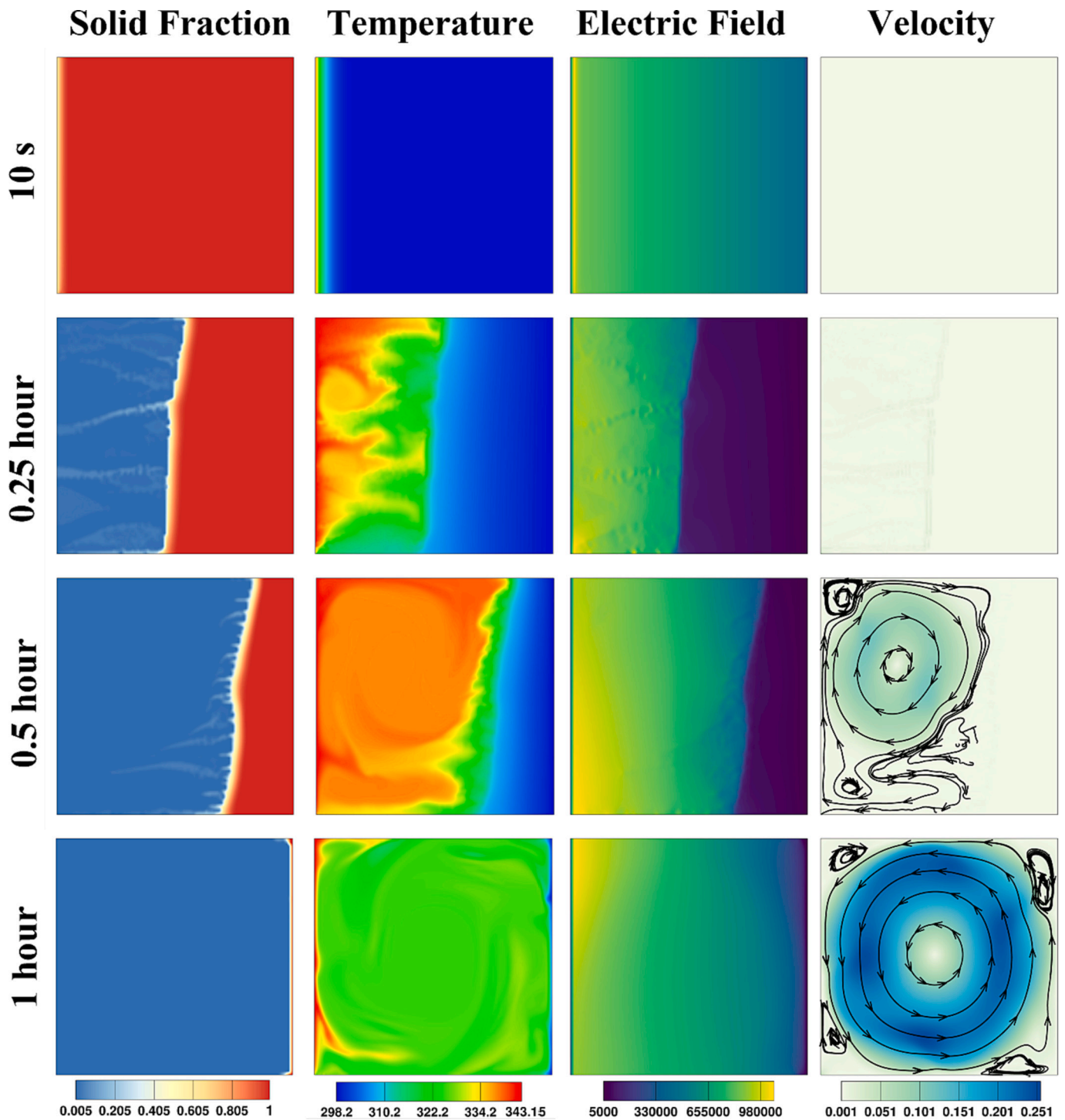


Fig. 14. Solid fraction distribution, thermal field, electric-field, and velocity at different instantaneous moments during the EHD-assisted melting of paraffin wax in a square capsule. The applied electric potential is 20 kV in a strong charge-injection regime ( $C = 10$ ).

indicates the onset of buoyancy-driven convection. The liquid PCM at high temperatures always tends to move toward the upper part of the cavity. Thus, the melting rate is enhanced in the top region, and the top end of the interface advances faster toward the right wall of the cavity. The onset of fluid motion is confirmed by the rise in the mean velocity, as seen in Fig. 7(b). At  $t = 1$  h, the melt interface notably leans toward the cold wall, and a well-defined single-cell flow structure is observed. As the melt interface moves away from the hot wall, the strength of the natural convection induced by the hot wall becomes weaker, as shown in the velocity-evolution curve in Fig. 7(b). This condition leads to thermal

stratification that causes the mean velocity and liquid fraction to approach an almost steady state. The contours at  $t = 4$  h show that a small amount of paraffin wax remains in the solid state near the bottom right corner, and a thin layer sticks to the cold wall. The flow structure is similar to natural convection in a differentially heated cavity except for the disturbance caused by the solid PCM that sticks to the right and bottom right corner. Thus, we can infer that the natural convection melting of the paraffin wax is characterized by conduction heat transfer for a very short period at the start of melting. Then, the onset of buoyancy flow leads to an inclined solid-liquid interface with a single-cell

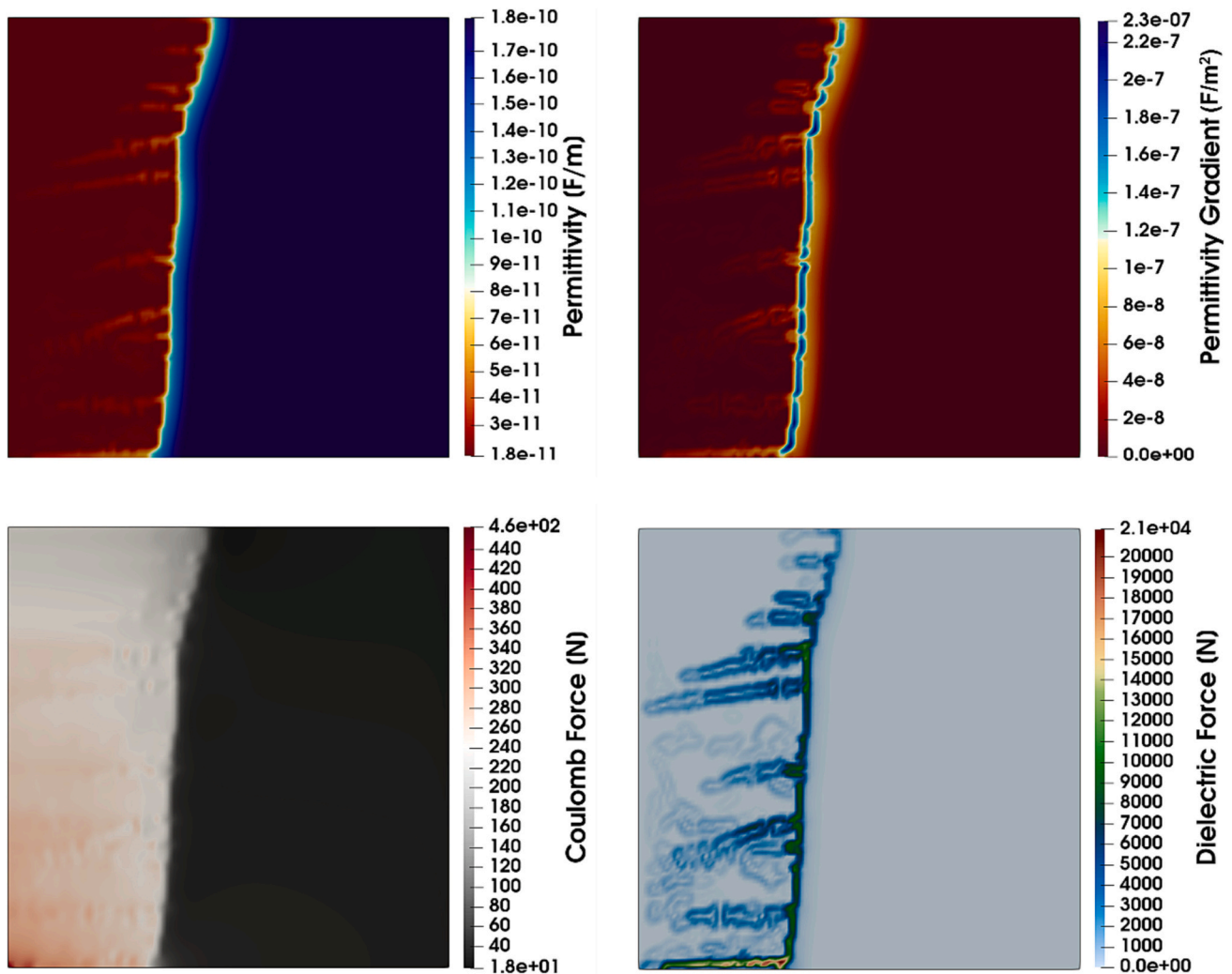


Fig. 15. Distribution of permittivity, permittivity gradient, Coulomb force and dielectric force in the flow domain at  $C = 10$  and  $V = 10$  kV.

flow structure. We need to note that the interface is not sharp, as observed in the case of isothermal melting [19]. Instead, the interface is thick and diffused because of the wider melting-temperature range of the paraffin wax. However, the interface has a defined shape determined by the natural convective flow cell. Because achieving 100 % melting is difficult, we consider 95 % melting as the benchmark for comparative analysis. Without an electric field, 95 % melting is achieved at  $t = 1.98$  h.

## 5.2. Mechanism of EHD assisted melting and solid extraction

To understand the EHD-assisted melting process, we consider the case under an applied voltage of 20 kV at the right cold wall. The left hot wall is grounded. Thus, charge injection takes place from the right wall toward the left wall. Weak, medium, and strong injection regimes with injection parameters  $C = 0.1, 1,$  and  $10$  are considered. The time-evolution curves of the liquid fraction, mean Coulomb force, mean dielectric force and mean velocity are shown in Figs. 8–11, respectively. For a very brief period at the start of melting, the time-evolution curves of the liquid fraction (Fig. 8) and mean velocity (Fig. 11) are precisely coincident with those in the case without an electric field, which marks the conduction-dominated period where no significant fluid flow occurs. A minimal liquid volume is seen very close to the solid wall during this period. The small liquid volume and its proximity to the solid wall restrict any significant fluid motion. The contours of the solid fraction,

temperature, electric field, and velocity under an applied voltage of 20 kV and in the weak, medium, and strong injection regimes are shown in Figs. 12–14, respectively. In the contours at  $t = 10$  s (first row in Figs. 12–14), we can observe that no liquid is present except for a skinny semi-solid layer near the hot wall. A temperature field, mainly due to conduction, and a smooth electric-field distribution, which is only due to the mobility of ions in the solid region, are observed. We must also note that the direction of the electric field is from left to right despite the high voltage applied at the right wall because of the lower permittivity of the liquid paraffin wax. The electric field is always higher in the liquid and semi-solid regions with lower permittivity than that in the solid region, which occurs in a very short time duration in the scale of charge-relaxation time ( $1 \times 10^{-4}$  s). At this point, no significant fluid flow occurs, as observed in the velocity contours.

At approximately  $t = 0.16$  s, the liquid-fraction curve in the cases with the electric field begins to deviate from that of the pure natural-convection-driven melting case. This deflection point in the melting-rate curve marks the onset of fluid motion. Corresponding to this deflection point, the curves of the mean Coulomb force (Fig. 9), mean dielectric force (Fig. 10) and mean velocity (Fig. 11) in the liquid region exhibit a sudden spike. The spikes in these curves are higher in stronger charge-injection regimes. Although the melting-rate curves in the weak, medium, and strong injection regimes shift from those of the case without an electric field, they coincide with one another during this period. This result can be explained in reference to the magnitude of the

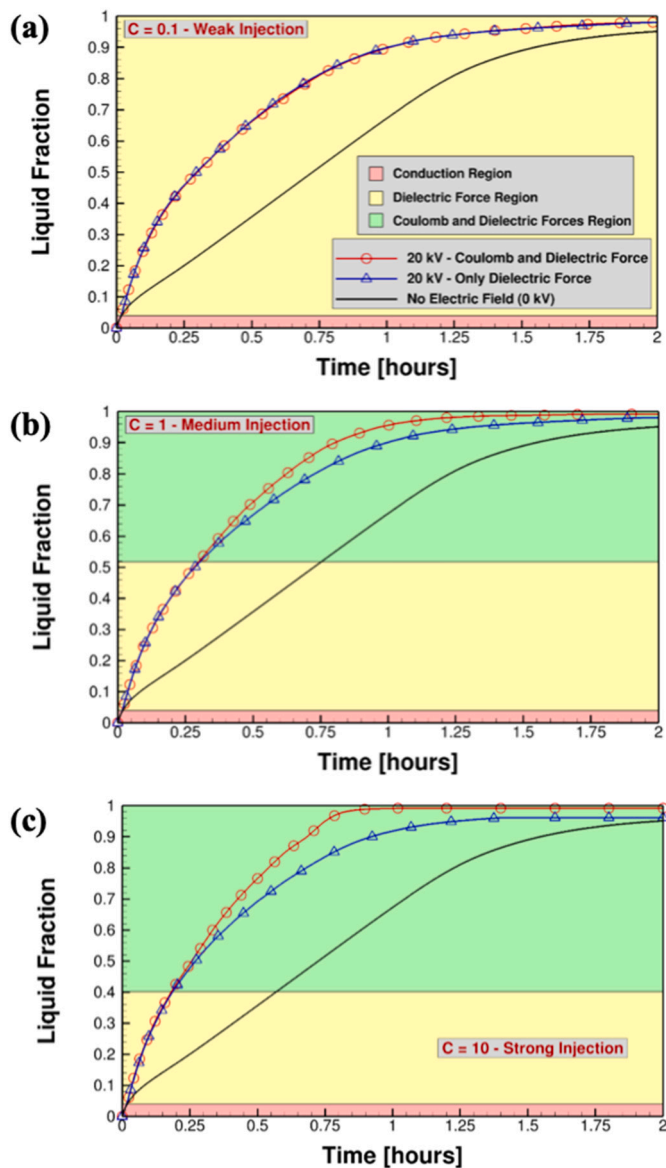


**Fig. 16.** Growth of liquid volume fraction during the EHD-assisted melting of paraffin wax with and without Coulomb force in (a) weak, (b) medium, and (c) strong injection regimes.

mean Coulomb and dielectric forces. The variations in the mean Coulomb force between each charge-injection regime are significant. However, the mean dielectric-force curves between each injection regime are not very different except for the first spike. In addition, the magnitude of the mean dielectric force is several times higher than that of the mean Coulomb force. Thus, the dielectric force primarily dictates the melting-rate enhancement in this period. The contours at  $t = 0.25$  h are shown in the second row in Figs. 12–14. The striking feature in the solid-fraction contours is the streaks of the semi-solid paraffin wax that extend from the interface into the liquid bulk region. As noted in the expression for dielectric force in Eq. (3), the dielectric force is a function of the permittivity gradient. The dielectric force will be zero in the regions without any permittivity gradient.

In the computational domain considered herein, the dielectric permittivity gradient exists only in the semi-solid interface region. Thus, the dielectric force acts only in the interface region, in a normal direction toward the region with strong electric field distribution. Electric field distribution in Figs. 12–14, show that electric field intensity is strong near the left heated wall. Thus, the dielectric force acts

horizontally in the interface, horizontally in right to left direction. As a result, the semi-solid paraffin wax in solid-liquid interface region is extracted into the liquid region with strong electric field. This phenomenon of the semi-solid mushy paraffin wax being drawn from the interface into the liquid bulk region is termed “solid extraction,” as reported for the first time by Nakhla et al. [10]. A synonymous observation of “liquid extraction” in the presence of an electric field in liquid-liquid multiphase systems is a well-documented phenomenon in literature [46–49]. The dendrites of the semi-solid paraffin wax undergo melting as they are pulled into the bulk liquid toward the hot wall. During this stage, the solid extraction phenomenon observed in the solid-fraction contours and the temperature, electric field, and velocity distributions is almost identical in all injection regimes. The dark stripes in the velocity field represent the disturbances in the flow field caused by the solid extraction phenomenon. The strips are darker in the weaker injection regimes because of the different scales of the velocity contours. We must note that the mean-velocity curves shown in Fig. 11 in all injection regimes are identical at  $t = 0.16$  s. Thus, we can infer that the charge-injection strength does not influence the solid extraction phenomenon at this stage.

When the melting process continues, the melting-rate curves in the different injection regimes begin to deviate from one another. We note that the melting rate in the cases with an electric field is already higher than those without an electric field. At this stage, the stronger injection regime exhibits a higher melting rate. At time  $t = 0.5$  h, we can observe that the mean-velocity curve (Fig. 11) in the strong injection regime is notably higher than in the medium and weak injection regimes. The mean-velocity curve in the medium injection regime is also slightly higher than in the weak injection regime. The mean Coulomb and dielectric forces can explain this result at this stage. The mean Coulomb force is higher in stronger charge-injection regimes, whereas the mean dielectric force at this point in time exhibits an inverse relationship with the charge-injection strength. The mean dielectric force is highest in the weak injection regime and lowest in the strong injection regime. The dendrites of semi-solid paraffin wax continuously moving toward the left wall result in the accumulation of charges over the left wall. This charge accumulation favors the Coulomb force and suppresses the dielectric force [10,50]. The charge accumulation over the left wall is stronger in stronger charge-injection regimes. Thus, the dielectric force is lower at stronger charge-injection strengths. At this stage, the mean Coulomb force is stronger than the dielectric force in the strong injection regime. The contours in Figs. 12 and 13 in the third row show that solid extraction remains evident in the weak and medium injection regimes. The solid extraction process also controls the flow and temperature fields, whereas convective flow cells with significantly higher velocities are observed in the strong injection regime. The solid extraction phenomenon is also suppressed by the onset of strong electroconvective flow due to the Coulomb force in strong charge injection regime. The thermal plumes also assume the shape of an electroconvective flow cell, which indicates that the electroconvective flow dictates the heat transfer at this stage. The Coulomb force begins to strongly influence the melting process in the strong injection regime at this stage. In contrast, its role is minimum in the medium injection regime and insignificant in the weak injection regime.

All cases approach thermal stratification in the later stage of the melting process. However, the maximum reachable liquid fraction is higher in the cases with an electric field. Thus, the electric field can help in overcoming thermal stratification. The mean-velocity curves are notably higher in the medium and strong injection regimes, whereas that in the weak injection regime is almost coincident with the case without an electric field. This result indicates the presence of electroconvective flow in the medium and strong injection regimes, as shown in the fourth row in Figs. 13 and 14. The mean dielectric-force curves in the medium and strong injection regimes almost approach zero. Thus, the solid extraction phenomenon is insignificant, and the flow and temperature fields are dictated by the electroconvective flow due to the

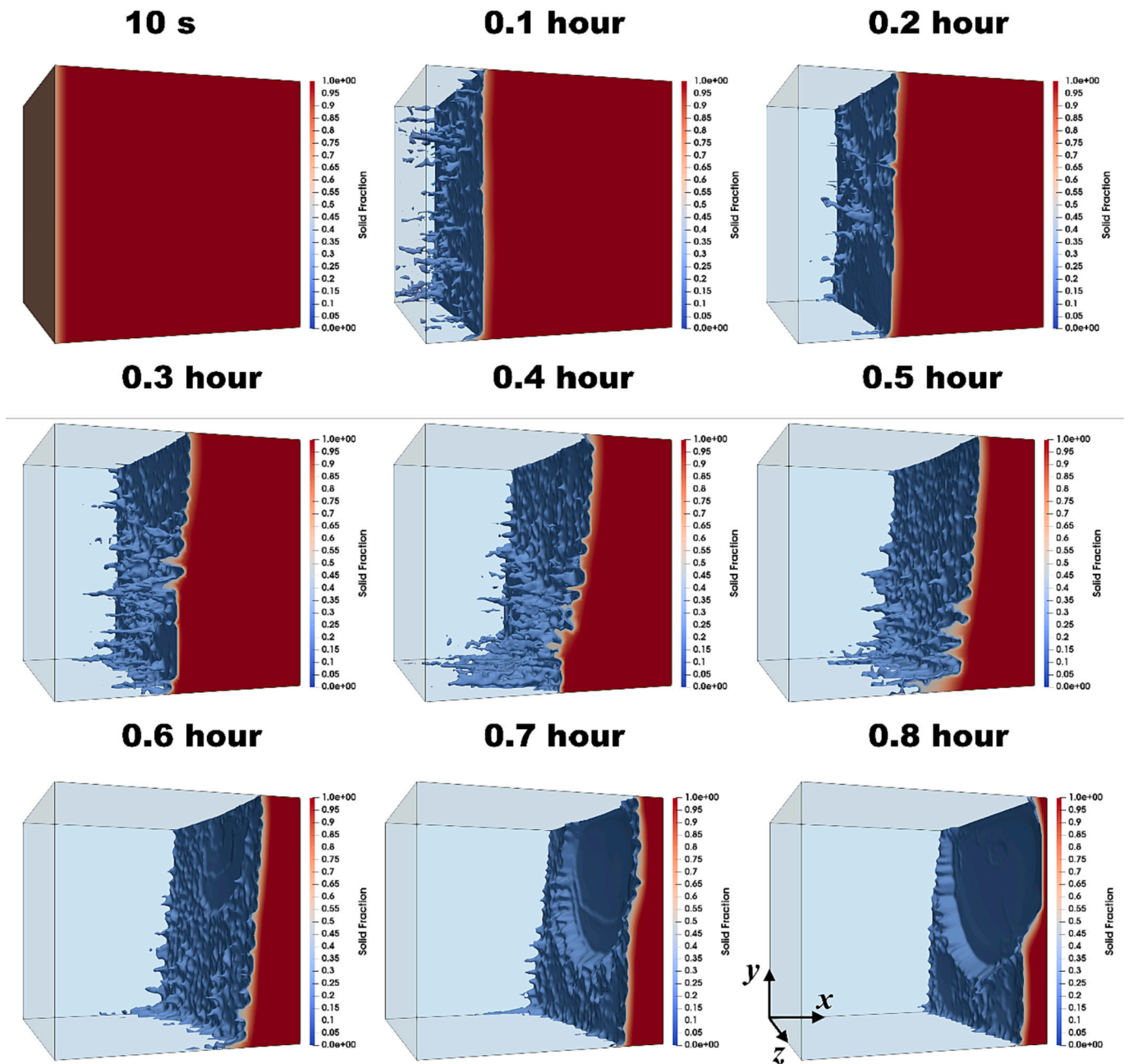


**Fig. 17.** Contours of the solid fraction during the EHD-assisted melting of paraffin wax in a 3D cubical capsule at an applied electric potential of 20 kV and strong injection regime ( $C = 10$ ).

Coulomb force.

In contrast, the dielectric force still plays a dominant role in the weak injection regime. Fig. 10 shows that the dielectric force in the weak injection regime is higher than those in the medium and strong injection regimes, which is also confirmed by the evident solid extraction phenomenon that remains visible in the contours of the solid fraction (fourth row in Fig. 12). Thus, the later stages of melting in the medium and strong injection regimes are also influenced by the electroconvective flow due to the Coulomb force. Meanwhile, the Coulomb force is insignificant in the weak injection regime throughout the melting process.

The mechanism of the solid extraction phenomenon observed in the cases described above is mainly attributed to the variation of dielectric permittivity and the resultant action of electric forces. Fig. 15 provides the distribution of dielectric permittivity, permittivity gradient,

Coulomb, and dielectric forces in the domain at 1000 s for the case of strong charge injection ( $C = 10$ ) and applied voltage  $V = 10$  kV. It is seen that the dielectric permittivity is distinct in the bulk solid and liquid regions. The permittivity changes as a function of liquid fraction in the mushy semi-solid region. As a result, we notice the permittivity gradient only along the interface and the streaks of semi-solid PCM pulled into the liquid bulk. From Eq. (3), we understand that the Coulomb force is independent of the permittivity gradient. Thus, the Coulomb force is smoothly distributed in the liquid bulk region. Minimal disturbances noticed in the distribution of the Coulomb force are due to the disturbances in the velocity field caused by the solid extraction. However, the dielectric force acts prominently along the interface, and the semi-solid PCM is pulled into the liquid bulk. From Eq. (3), it is clear that the dielectric force is a function of gradient in dielectric permittivity. Thus, it is confirmed that the solid extraction phenomenon results from the

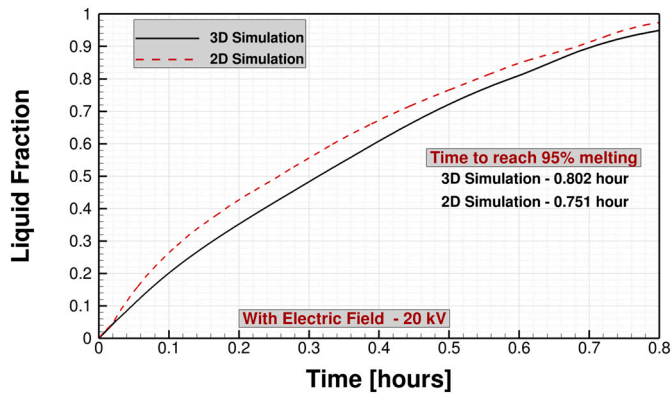


Fig. 18. Growth of liquid volume fraction in EHD-assisted melting in a square capsule using 2D and 3D domains at an applied electric potential of 20 kV and strong injection regime ( $C = 10$ ).

Table 3 Summary of the melting-time reduction in the EHD-assisted melting of paraffin wax in a square cavity.

| Charge-injection regime | Applied electric potential [kV] | Time to reach 95 % melting [hours] | % Reduction in melting time |
|-------------------------|---------------------------------|------------------------------------|-----------------------------|
| $C = 0.1$ (Weak)        | 0                               | 1.98                               | –                           |
|                         | 10                              | 1.94                               | 2.02                        |
|                         | 20                              | 1.35                               | 31.81                       |
| $C = 1$ (Medium)        | 0                               | 1.98                               | –                           |
|                         | 10                              | 1.81                               | 8.59                        |
|                         | 20                              | 0.97                               | 51.01                       |
| $C = 10$ (Strong)       | 0                               | 1.98                               | –                           |
|                         | 10                              | 1.14                               | 42.42                       |
|                         | 20                              | 0.75                               | 62.12                       |

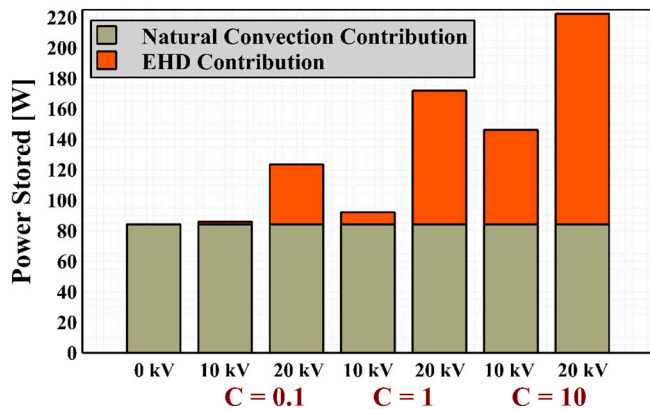


Fig. 19. Total power stored at the stage of 95 % melting for  $C = 0.1, 1$  and  $10$  at applied voltages 0, 10 and 20 kV.

Table 4 Average electric power consumption in cases considered in this study.

| $C = 0.1$ (Weak)                |                                 | $C = 1$ (Medium)                |                                 | $C = 10$ (Strong)               |                                 |
|---------------------------------|---------------------------------|---------------------------------|---------------------------------|---------------------------------|---------------------------------|
| Applied electric potential [kV] | Electric power consumption [mW] | Applied electric potential [kV] | Electric power consumption [mW] | Applied electric potential [kV] | Electric power consumption [mW] |
| 10                              | 0.63                            | 10                              | 1.01                            | 10                              | 1.83                            |
| 20                              | 1.25                            | 20                              | 2.11                            | 20                              | 3.61                            |

action of dielectric force due to the gradient in permittivity.

### 5.3. Role of coulomb and dielectric forces

Two sets of cases are simulated to provide further insights into the role of the Coulomb and dielectric forces in the weak, medium, and strong injection regimes. The first case considers the effect of both the Coulomb and dielectric forces. The second case considers only the dielectric force. The time-evolution curves of the liquid fraction obtained in both cases at an applied voltage of 20 kV in the weak, medium, and strong injection regimes are shown in Fig. 16(a)–(c). The curve in the case without an electric field is also shown for reference. In all injection regimes, we observe that the cases with an electric field deviated from the curve compared with that without an electric field. Thus, applying an electric field generally enhances the melting process. In all three injection regimes, a very short period exists at the start of the melting process, where the curves in the cases with an electric field coincide with those without an electric field. This short period marks the conduction-dominated region, shown in the red shade in Fig. 16(a)–(c). This conduction-dominated region is identical in all injection strengths. Following the short conduction-dominated period, the melting-rate curves in the cases with an electric field begin to deviate from those in the case without an electric field. At this stage, the curves with and without Coulomb force are identical, which indicates that the enhancement in the melting rate observed during this stage is only caused by the dielectric force and resultant solid extraction phenomenon. This is the dielectric-force-dominated region shown in the yellow shade in Fig. 16(a)–(c).

In the weak injection regime, the curves in the cases with and without a Coulomb force are identical until the end of the melting process. Thus, we can infer that the dielectric force solely induces the melting enhancement in the weak injection regime. In the medium and strong injection regimes, a third stage exists where the curves in the cases with and without a Coulomb force deviate from each other. In the absence of the Coulomb force, the melting-rate curves slightly decrease compared with those in the case with both the Coulomb and dielectric forces. Thus, in this stage, the melting-rate enhancement results from the combined action of the Coulomb and dielectric forces. The decrease in the melting rate due to the absence of the Coulomb force is slightly higher in the strong injection regime. Hence, in the medium and strong injection regimes, a third stage exists, which is influenced by the combined action of the Coulomb and dielectric forces [shown in the green shade in Figs. 16(b) and (c)]. In all injection regimes, the conduction-dominated region is observed up to 3 % of the liquid fraction. In the weak injection regime, the dielectric-force-dominated region is observed from 3 % melting to almost the entire melting process. In the medium injection regime, the dielectric-force-dominated regime ranges from 3 % to 52 % melting, and the remaining melting process exhibits the combined action of the Coulomb and dielectric forces. In the strong injection regime, the dielectric-force-dominated region ranges from 3 % to 40 % of the melting process. The Coulomb and dielectric forces influence the remaining melting process.

### 5.4. 3D visualization of solid extraction phenomenon

To investigate the three-dimensionality of the EHD-assisted melting process and provide better visualization of the solid extraction phe-

nomenon, a 3D simulation is performed for the case where  $C = 10$  and  $V_0 = 20$  kV. A  $150 \times 150 \times 150$  uniform grid is employed in this 3D simulation. The 3D contours of the solid fraction at different progressive time steps are shown in Fig. 17. As previously explained, the melting process begins with conduction followed by significant solid extraction due to the dielectric force. We can observe semi-solid dendrites of paraffin wax extracted from the interface toward the liquid bulk region under a high electric field. The perpendicular nature of these dendrites confirms the dielectric force that acts normal to the interface toward the bulk liquid region. At the later stages of melting, the solid extraction phenomenon becomes weak, and a circular dip in the interface is observed. This condition illustrates the electroconvective flow caused by the Coulomb force. The interface takes the shape of the electroconvective flow cell. We need to mention that the two-dimensionality of the problem is considered based on the symmetry of the interface in the  $z$ -direction. However, the 3D simulation demonstrates that the interface exhibits a slight asymmetry in the  $z$ -direction. The melting-rate curves of the 2D and 3D simulations are compared, as shown in Fig. 18. We can observe that the 2D simulation leads to a slight over-prediction in the melting-rate enhancement. However, the overall process follows a similar trend. The difference in the time taken to reach 95 % melting between the 2D and 3D simulations is approximately 6.4 %. We also have to note that the grid density used in the 3D simulation is lower than that used in the 2D simulation.

### 5.5. Performance evaluation

A summary of the reduction in the melting times observed in the three injection regimes and two levels of applied voltages is listed in Table 3. All cases are compared with respect to the time taken to reach 95 % melting. In general, the application of an external electric field leads to a reduction in the melting time. Higher applied electric potential leads to higher enhancement in the melting process in all injection regimes. The stronger the charge injection is, the higher the reduction in the melting time. For the parameters considered in this study, a maximum of 62.12 % decrease in the melting time is observed at  $C = 10$  and  $V_0 = 20$  kV. The net power stored during the melting process is expressed as [51].

$$\text{Net power stored } POW = \frac{[m_l \cdot (C_{pl} \cdot (T_l - T_\infty) + L)] + [m_s \cdot C_{ps} \cdot (T_s - T_\infty)]}{\text{Time required to reach 95\% melting}} \quad (21)$$

Here, the mass of liquid and solid PCM at the stage of 95 % melting is denoted by  $m_l$  and  $m_s$ , respectively.  $T_l$  and  $T_s$  are the mean temperatures of the liquid and solid phases at 95 % melting. The first term in the numerator gives the net heat stored in the liquid PCM.  $m_l \cdot (C_{pl} \cdot (T_l - T_\infty))$  is the sensible heat content stored in liquid phase and the latent heat content stored in liquid phase is given by  $m_l \cdot L$ . The total sensible heat stored in the solid phase is given by  $m_s \cdot C_{ps} \cdot (T_s - T_\infty)$ . The total power stored in each case considered in this study is presented in Fig. 19. In the case without electric field, the power stored when the system reaches 95 % melting is 84.21 W. At a given charge injection strength, increase in applied voltage leads to higher power storage. Similarly, for a given applied voltage, increasing the charge injection strength provides higher power storage. The highest total power storage of 222.31 W is achieved at  $C = 10$  and at an applied voltage of 20 kV.

From the results presented in this study, it is evident that the application of EHD flow accelerates the melting process. However, there will be additional power requirement for inducing the EHD flow. The additional electric power consumption for the EHD flow is calculated as  $P_{EL} = V \times I$ .  $V$  is the applied voltage and  $I_{tot}$  is the instantaneous current passing the system which is calculated as

$$I = \iint \left[ \vec{J} + \frac{\partial \vec{E}}{\partial t} \right] \cdot \hat{n} dS \quad (22)$$

The total current consumed in each case until 95 % melting is considered. The electric power consumption in each case is provided in Table 4. The electric power consumption for the generation of the EHD flow in all of the cases is in the order of few milliwatts. The average heat power supplied in the left wall is around 1.168 W. While the maximum electric power consumption noted among the cases considered in this study is 3.61 mW. Thus, the unipolar charge injection induced by an external electric field is a viable economic option for enhancing the solid-liquid phase-change processes encountered in LHTES systems.

## 6. Concluding remarks

A numerical analysis of EHD assisted non-isothermal melting of PCM in a square cavity has been presented. The effects of charge injection strength on EHD assisted melting process are presented for the first time in literature. This study numerically demonstrates the solid extraction phenomenon observed in the EHD-assisted melting of paraffin wax. The role of the Coulomb and dielectric forces at different stages of the melting process and different injection regimes is quantified. The concluding inferences drawn from the numerical analysis are listed as follows:

- EHD flow increases the fluid mixing and heat transfer in the liquid region and the melting rate.
- Higher applied voltage leads to shorter melting times at any given charge injection regime.
- The EHD flow intensity is higher at stronger charge injection regimes. Thus, the rate of melting is higher for stronger charge injection.
- The interface region experiences a change in permittivity distribution. Thus, the dielectric force acts on the semi-solid PCM in the interface and leads to the solid extraction phenomenon.
- In the weak injection regime, the role of the Coulomb force is insignificant. The melting enhancement is solely due to the solid extraction phenomenon caused by the dielectric force.
- In the medium and strong injection regimes, the dielectric force entirely dominates the first half of the EHD-assisted melting process. The combination of the Coulomb and dielectric forces influences the second half of the EHD-assisted melting process.
- A maximum of 62.12 % reduction in melting time is achieved in the considered parameter space.
- Net power stored during the melting process is higher for the cases with the electric field compared to pure natural convection melting.
- The maximum increase in power storage obtained is 138.1 W, whereas the corresponding additional electric power consumption is only 3.61 mW. Thus, minimal additional electric energy expenditure obtains a notable increase in thermal power storage.

## Declaration of competing interest

The authors declare that they have no known competing financial interests or personal relationships that could have appeared to influence the work reported in this paper.

## Data availability

Data will be made available on request.

## Acknowledgments

This research was supported by the Chung-Ang University Research Grants in 2021. One of the authors acknowledge the financial support from Khalifa University of Science and Technology (KUST), United Arab Emirates under Award No. CIRA-2021-066.

## CRediT authorship contribution statement

**R.Deepak Selvakumar:** Data curation, Formal Analysis, Investigation, Methodology, Writing-Original Draft, Preparation. **Ahmed K. Alkaabi:** Supervision, Funding acquisition. **Jaiyoung Ryu:** Supervision, Writing-review & editing. **Hyungsoon Lee:** Supervision, Writing-review & editing, Funding acquisition.

## References

- [1] A. Sharma, V.V. Tyagi, C.R. Chen, D. Buddhi, Review on thermal energy storage with phase change materials and applications, *Renew. Sust. Energ. Rev.* 13 (2009) 318–345, <https://doi.org/10.1016/j.rser.2007.10.005>.
- [2] D. Zhou, C.Y. Zhao, Y. Tian, Review on thermal energy storage with phase change materials (PCMs) in building applications, *Appl. Energy* 92 (2012) 593–605, <https://doi.org/10.1016/j.apenergy.2011.08.025>.
- [3] S. Jegadheeswaran, S.D. Pohekar, Performance enhancement in latent heat thermal storage system: a review, *Renew. Sust. Energ. Rev.* 13 (2009) 2225–2244, <https://doi.org/10.1016/j.rser.2009.06.024>.
- [4] A.F. Regin, S.C. Solanki, J.S. Saini, Heat transfer characteristics of thermal energy storage system using PCM capsules: a review, *Renew. Sust. Energ. Rev.* 12 (2008) 2438–2458, <https://doi.org/10.1016/j.rser.2007.06.009>.
- [5] S. Jegadheeswaran, S.D. Pohekar, Performance enhancement in latent heat thermal storage system: a review, *Renew. Sust. Energ. Rev.* 13 (2009) 2225–2244, <https://doi.org/10.1016/j.rser.2009.06.024>.
- [6] A. Castellanos, Coulomb-driven convection in electrohydrodynamics, *IEEE Trans. Electr. Insul.* 26 (1991) 1201–1215, <https://doi.org/10.1109/14.108160>.
- [7] S. Rashidi, H. Bafekr, R. Masoodi, E.M. Languri, EHD in thermal energy systems - a review of the applications, modelling, and experiments, *J. Electrostat.* 90 (2017) 1–14, <https://doi.org/10.1016/j.elstat.2017.08.008>.
- [8] R.D. Selvakumar, H. Lee, Bouncing modes and heat transfer of a dielectric droplet in the presence of an external electric field, *Int. J. Heat Mass Transf.* 191 (2022) 122837, <https://doi.org/10.1016/j.ijheatmasstransfer.2022.122837>.
- [9] Y. Kim, S. Jung, S. Kim, S.T. Choi, M. Kim, H. Lee, Heat transfer performance of water-based electrospray cooling, *Int. Commun. Heat Mass Transf.* 118 (2020) 104861, <https://doi.org/10.1016/j.icheatmasstransfer.2020.104861>.
- [10] D. Nakhla, H. Sadek, J.S. Cotton, Melting performance enhancement in latent heat storage module using solid extraction electrohydrodynamics (EHD), *Int. J. Heat Mass Transf.* 81 (2015) 695–704, <https://doi.org/10.1016/j.ijheatmasstransfer.2014.10.016>.
- [11] D. Nakhla, J.S. Cotton, Effect of electrohydrodynamic (EHD) forces on charging of a vertical latent heat thermal storage module filled with octadecane, *Int. J. Heat Mass Transf.* 167 (2021) 120828, <https://doi.org/10.1016/j.ijheatmasstransfer.2020.120828>.
- [12] D. Nakhla, E. Thompson, B. Lacroix, J.S. Cotton, Measurement of heat transfer enhancement in melting of n-Octadecane under gravitational and electrohydrodynamics (EHD) forces, *J. Electrostat.* 92 (2018) 31–37, <https://doi.org/10.1016/j.elstat.2018.01.004>.
- [13] A. Hassan, J.S. Cotton, Investigation of the role of electrohydrodynamic forces on the heat transfer enhancement and solid extraction during melting of paraffin wax under constant temperature boundary conditions, *Int. J. Heat Mass Transf.* 204 (2023) 123831, <https://doi.org/10.1016/j.ijheatmasstransfer.2022.123831>.
- [14] Z. Sun, P. Yang, K. Luo, J. Wu, Experimental investigation on the melting characteristics of n-octadecane with electric field inside macrocapsule, *Int. J. Heat Mass Transf.* 173 (2021) 121238, <https://doi.org/10.1016/j.ijheatmasstransfer.2021.121238>.
- [15] K. Luo, A.T. Pérez, J. Wu, H.-L. Yi, H.-P. Tan, Efficient lattice Boltzmann method for electrohydrodynamic solid-liquid phase change, *Phys. Rev. E* 100 (2019), 013306, <https://doi.org/10.1103/PhysRevE.100.013306>.
- [16] C.-L. Lu, K. Luo, P.-C. Zhou, H.-L. Yi, Lattice Boltzmann analysis for electro-thermo-convection with a melting boundary in horizontal concentric annuli, *Phys. Fluids* 33 (2021) 43605, <https://doi.org/10.1063/5.0046975>.
- [17] C.-L. Lu, K. Luo, P.-C. Zhou, H.-L. Yi, Rayleigh-Bénard convection in a dielectric fluid under an external electric field with a melting boundary, *Phys. Rev. Fluids* 6 (2021) 63504.
- [18] C.-L. Lu, X.-L. Gao, J. Wu, K. Luo, H.-L. Yi, Heat transfer enhancement analysis of electrohydrodynamic solid-liquid phase change via lattice Boltzmann method, *Appl. Therm. Eng.* 117112 (2021).
- [19] R.D. Selvakumar, L. Qiang, L. Kang, P. Traoré, J. Wu, Numerical modeling of solid-liquid phase change under the influence an external electric field, *Int. J. Multiphase Flow* 136 (2021), <https://doi.org/10.1016/j.ijmultiphaseflow.2020.103550>.
- [20] R.D. Selvakumar, S. Vengadesan, Combined effects of buoyancy and electric forces on non-isothermal melting of a dielectric phase change material, *Int. J. Multiphase Flow* (2022) 104029, <https://doi.org/10.1016/j.ijmultiphaseflow.2022.104029>.
- [21] R.D. Selvakumar, J. Wu, I. Afgan, Y. Ding, A.K. Alkaabi, Melting performance enhancement in a thermal energy storage unit using active vortex generation by electric field, *J. Energy Storage* 67 (2023) 107593, <https://doi.org/10.1016/j.est.2023.107593>.
- [22] R. Deepak Selvakumar, J. Wu, Y. Ding, A.K. Alkaabi, Melting behavior of an organic phase change material in a square thermal energy storage capsule with an array of wire electrodes, *Appl. Therm. Eng.* 228 (2023) 120492, <https://doi.org/10.1016/j.applthermaleng.2023.120492>.
- [23] H.E. Endigeri, R. Deepak Selvakumar, S. Vengadesan, Solid-liquid phase change subjected to unipolar charge injection from a circular wire electrode, *Int. J. Heat Mass Transf.* 194 (2022) 123120, <https://doi.org/10.1016/j.ijheatmasstransfer.2022.123120>.
- [24] Z. Sun, K. Luo, J. Wu, Experimental study on the melting characteristics of n-octadecane with passively installing fin and actively applying electric field, *Int. Commun. Heat Mass Transf.* 127 (2021) 105570, <https://doi.org/10.1016/j.icheatmasstransfer.2021.105570>.
- [25] Z. Sun, Y. Zhang, K. Luo, A.T. Pérez, H. Yi, J. Wu, Experimental investigation on melting heat transfer of an organic material under electric field, *Exp. Thermal Fluid Sci.* 131 (2022) 110530, <https://doi.org/10.1016/j.expthermflusci.2021.110530>.
- [26] K. Luo, J. Wu, A.T. Pérez, H.-L. Yi, H.-P. Tan, Stability analysis of electroconvection with a solid-liquid interface via the lattice Boltzmann method, *Phys. Rev. Fluids* 4 (2019) 83702.
- [27] F.M.J. McCluskey, P. Atten, A.T. Perez, Heat transfer enhancement by electroconvection resulting from an injected space charge between parallel plates, *Int. J. Heat Mass Transf.* 34 (1991) 2237–2250, [https://doi.org/10.1016/0017-9310\(91\)90050-O](https://doi.org/10.1016/0017-9310(91)90050-O).
- [28] P.H. Traoré, A.T. Pérez, D. Koulova, H. Romat, Numerical modelling of finite-amplitude electro-thermo-convection in a dielectric liquid layer subjected to both unipolar injection and temperature gradient, *J. Fluid Mech.* 658 (2010) 279–293, <https://doi.org/10.1017/S0022112010001709>.
- [29] J. Wu, P. Traoré, A finite-volume method for electro-thermoconvective phenomena in a plane layer of dielectric liquid, *Num. Heat Transf. A Appl.* 68 (2015) 471–500, <https://doi.org/10.1080/10407782.2014.986410>.
- [30] P. Atten, F.M.J. McCluskey, A.T. Perez, Electroconvection and its effect on heat transfer, *IEEE Trans. Electr. Insul.* 23 (1988) 659–667, <https://doi.org/10.1109/14.7338>.
- [31] A.D. Brent, V.R. Voller, K.J. Reid, Enthalpy-porosity technique for modeling convection-diffusion phase change: application to the melting of a pure metal, *Num. Heat Transf.* 13 (1988) 297–318, <https://doi.org/10.1080/10407788808913615>.
- [32] D. Ghosh, C. Guha, Numerical simulation of paraffin wax melting in a rectangular cavity using CFD, *Indian Chem. Eng.* 62 (2020) 314–328, <https://doi.org/10.1080/00194506.2019.1689183>.
- [33] C. Huber, A. Parmigiani, B. Chopard, M. Manga, O. Bachmann, Lattice Boltzmann model for melting with natural convection, *Int. J. Heat Fluid Flow* 29 (2008) 1469–1480.
- [34] M. Faden, A. König-Haagen, D. Brüggemann, An optimum enthalpy approach for melting and solidification with volume change, *Energies (Basel)* 12 (2019), <https://doi.org/10.3390/en12050868>.
- [35] D.A. Nield, A. Bejan, *Convection in Porous Media*, Springer, 2006.
- [36] C.A. Saleel, Numerical study on melting and heat transfer characteristics of paraffin wax/ SiC paraffin using enthalpy-porosity model, *J. Therm. Anal. Calorim.* (2022), <https://doi.org/10.1007/s10973-022-11265-z>.
- [37] D. Nakhla, Characterization of Electrohydrodynamic (EHD) Heat Transfer Enhancement Mechanisms in Melting of Organic Phase Change Material (PCM), *McMaster University*, 2018.
- [38] I. Adamczewski, J.H. Calderwood, Viscosity and charge carrier mobility in the saturated hydrocarbons, *J. Phys. D: Appl. Phys.* 8 (1975) 1211–1218, <https://doi.org/10.1088/0022-3727/8/10/009>.
- [39] P.R. Dellorusso, Electrohydrodynamic heat transfer enhancement for a latent heat storage heat exchanger, in: *DalTech-Dalhousie University*, 1999.
- [40] F. Moukalled, L. Mangani, M. Darwish, et al., *The finite volume method in computational fluid dynamics, an advanced introduction with OpenFoam® and Matlab®*, in: Nueva York: Springer. Recuperado de <http://www.Gidropraktikum.Narod.Ru/Moukalled-et-al-FVM-OpenFoam-Matlab>. Pdf, 2016.
- [41] B. van Leer, Towards the ultimate conservative difference scheme, *J. Comput. Phys.* 135 (1997) 229–248, <https://doi.org/10.1006/jcph.1997.5704>.
- [42] M. Faden, C. Linhardt, S. Höhle, A. König-Haagen, D. Brüggemann, Velocity field and phase boundary measurements during melting of n-octadecane in a cubical test cell, *Int. J. Heat Mass Transf.* 135 (2019) 104–114, <https://doi.org/10.1016/j.ijheatmasstransfer.2019.01.056>.
- [43] H. Shokouhmand, B. Kamkari, Experimental investigation on melting heat transfer characteristics of lauric acid in a rectangular thermal storage unit, *Exp. Thermal Fluid Sci.* 50 (2013) 201–212, <https://doi.org/10.1016/j.expthermflusci.2013.06.010>.
- [44] A. Mourad, A. Aissa, A.M. Abed, G.F. Smaism, D. Toghraie, M.A. Fazilati, O. Younis, K. Guedri, A. Alizadeh, The numerical analysis of the melting process in a modified shell-and-tube phase change material heat storage system, *J. Energy Storage* 55 (2022) 105827, <https://doi.org/10.1016/j.est.2022.105827>.
- [45] M.S. Mahdi, A.F. Hasan, H.B. Mahood, A.N. Campbell, A.A. Khadom, A.M. A. Karim, A.O. Sharif, Numerical study and experimental validation of the effects of orientation and configuration on melting in a latent heat thermal storage unit, *J. Energy Storage* 23 (2019) 456–468, <https://doi.org/10.1016/j.est.2019.04.013>.
- [46] Ryoichi Hanaoka, Yoji Fujita, Takuma Kajiuira, Hidenobu Anzai, Dynamic behavior and its consideration of EHD liquid extraction phenomenon causing under DC or low-frequency AC voltage, *J. Energy Power Eng.* 13 (2019), <https://doi.org/10.17265/1934-8975/2019.06.002>.
- [47] G.J. McGranaghan, A.J. Robinson, The mechanisms of heat transfer during convective boiling under the influence of AC electric fields, *Int. J. Heat Mass Transf.* 73 (2014) 376–388, <https://doi.org/10.1016/j.ijheatmasstransfer.2014.01.050>.
- [48] G. McGranaghan, A.J. Robinson, EHD augmented convective boiling: flow regimes and enhanced heat transfer, *Heat Transf. Eng.* 35 (2014) 517–527, <https://doi.org/10.1080/01457632.2013.833054>.

- [49] K. Cheung, M.M. Ohadi, S.V. Dessiatoun, EHD-assisted external condensation of R-134a on smooth horizontal and vertical tubes, *Int. J. Heat Mass Transf.* 42 (1999) 1747–1755, [https://doi.org/10.1016/S0017-9310\(98\)00291-9](https://doi.org/10.1016/S0017-9310(98)00291-9).
- [50] H.A. Pohl, Nonuniform field effects in poorly conducting media, *J. Electrochem. Soc.* 107 (1960) 386.
- [51] N.I. Ibrahim, F.A. Al-Sulaiman, S. Rahman, B.S. Yilbas, A.Z. Sahin, Heat transfer enhancement of phase change materials for thermal energy storage applications: a critical review, *Renew. Sust. Energ. Rev.* 74 (2017) 26–50, <https://doi.org/10.1016/j.rser.2017.01.169>.